The Astrophysical Journal Supplement Series, 246:48 (9pp), 2020 February https://doi.org/10.3847/1538-4365/ab5dae

Enhanced Energy Transfer Rate in Solar Wind Turbulence Observed near the Sun from *Parker Solar Probe*

Riddhi Bandyopadhyay[1], M. L. Goldstein[2,3], B. A. Maruca[1], W. H. Matthaeus[1], T. N. Parashar[1], D. Ruffolo[4], R. Chhiber[1,2], A. Usmanov[1,2], A. Chasapis[5], R. Qudsi[1], Stuart D. Bale[6,7,8,9], J. W. Bonnell[7], Thierry Dudok de Wit[10], Keith Goetz[11], Peter R. Harvey[7], Robert J. MacDowall[12], David M. Malaspina[13], Marc Pulupa[7], J. C. Kasper[14,15], K. E. Korreck[15], A. W. Case[15], M. Stevens[15], P. Whittlesey[16], D. Larson[16], R. Livi[16], K. G. Klein[17], M. Velli[18], and N. Raouafi[19]

[1] Department of Physics and Astronomy, Bartol Research Institute, University of Delaware, Newark, DE 19716, USA; riddhib@udel.edu
[2] NASA Goddard Space Flight Center, Greenbelt, MD 20771, USA
[3] University of Maryland Baltimore County, Baltimore, MD 21250, USA
[4] Department of Physics, Faculty of Science, Mahidol University, Bangkok 10400, Thailand
[5] Laboratory for Atmospheric and Space Physics, University of Colorado Boulder, Boulder, CO 80303, USA
[6] Physics Department, University of California, Berkeley, CA 94720-7300, USA
[7] Space Sciences Laboratory, University of California, Berkeley, CA 94720-7450, USA
[8] The Blackett Laboratory, Imperial College London, London, SW7 2AZ, UK
[9] School of Physics and Astronomy, Queen Mary University of London, London E1 4NS, UK
[10] LPC2E, CNRS and University of Orléans, Orléans, France
[11] School of Physics and Astronomy, University of Minnesota, Minneapolis, MN 55455, USA
[12] Solar System Exploration Division, NASA/Goddard Space Flight Center, Greenbelt, MD 20771, USA
[13] Laboratory for Atmospheric and Space Physics, University of Colorado, Boulder, CO 80303, USA
[14] Climate and Space Sciences and Engineering, University of Michigan, Ann Arbor, MI 48109, USA
[15] Smithsonian Astrophysical Observatory, Cambridge, MA 02138, USA
[16] University of California, Berkeley: Berkeley, CA, USA
[17] Lunar and Planetary Laboratory, University of Arizona, Tucson, AZ 85719, USA
[18] Department of Earth, Planetary, and Space Sciences, University of California, Los Angeles, CA 90095, USA
[19] Johns Hopkins University Applied Physics Laboratory, Laurel, MD 20723, USA
Received 2019 September 14; revised 2019 November 29; accepted 2019 November 29; published 2020 February 3

Abstract

Direct evidence of an inertial-range turbulent energy cascade has been provided by spacecraft observations in heliospheric plasmas. In the solar wind, the average value of the derived heating rate near 1 au is $\sim 10^3$ J kg^{-1} s^{-1}, an amount sufficient to account for observed departures from adiabatic expansion. *Parker Solar Probe*, even during its first solar encounter, offers the first opportunity to compute, in a similar fashion, a fluid-scale energy decay rate, much closer to the solar corona than any prior in situ observations. Using the Politano–Pouquet third-order law and the von Kármán decay law, we estimate the fluid-range energy transfer rate in the inner heliosphere, at heliocentric distance R ranging from 54 $R_\odot$ (0.25 au) to 36 $R_\odot$ (0.17 au). The energy transfer rate obtained near the first perihelion is about 100 times higher than the average value at 1 au, which is in agreement with estimates based on a heliospheric turbulence transport model. This dramatic increase in the heating rate is unprecedented in previous solar wind observations, including those from *Helios*, and the values are close to those obtained in the shocked plasma inside the terrestrial magnetosheath.

Unified Astronomy Thesaurus concepts: Interplanetary turbulence (829); Solar wind (1534); Magnetohydrodynamics (1964)

1. Introduction

A fundamental characteristic of a well-developed turbulent system is the transfer of energy from large length scales to small-scale structures, i.e., a turbulent energy cascade. The largest structures, known as the "energy-containing eddies," can be thought of as a reservoir of energy that injects energy into a broadband scale-to-scale transfer process. Assuming homogeneous and stationary fluctuations at these length scales, and a similarity law for turbulence evolution, de Kármán & Howarth (1938) develop a phenomenology to quantify the energy decay rate for moderate to high Reynolds-number flows. Here, as a first step, we employ a von Kármán law, generalized to magnetohydrodynamics (MHD; Wan et al. 2012; Bandyopadhyay et al. 2018b, 2019), for evaluating an approximate estimate of the large-scale energy decay rate close to the Sun.

For the next stage of turbulence transfer, at the inertial-range scales, Kolmogorov (1941) hypothesized a constant transfer of energy across scales, once again assuming idealized conditions. The associated scale-invariant energy flux has been measured in fluid as well as MHD simulations (Verma 2004). For in situ observations, the Kolomogorov–Yaglom law, generalized to MHD (Politano & Pouquet 1998a, 1998b), provides a practical way of computing the inertial-range energy cascade rate, directly. The Politano–Pouquet third-order law (Politano & Pouquet 1998a, 1998b), has been established as a rather satisfactory methodology for space plasma observations (MacBride et al. 2005, 2008; Sorriso-Valvo et al. 2007; Stawarz et al. 2009). The same formalism, as well as several generalizations, have been applied to numerical simulations (Mininni & Pouquet 2009).

At scales approaching the ion-gyro radius or ion-inertial length, an MHD description is not valid. Kinetic effects

become important near these small scales in a weakly collisional plasma such as the solar wind, and the energy cascade process becomes increasingly more complex. Several channels of energy conversion become available, dispersive plasma processes enter the description, and dissipation processes become progressively more important. A full understanding of the energy dissipation process and pathways at kinetic scales is far from complete at this stage and beyond the scope of the present discussion (Klein et al. 2017; Yang et al. 2017; Bandyopadhyay et al. 2018a; Hellinger et al. 2018; Chen et al. 2019). Nevertheless, if the system is evolving sufficiently slowly, one expects that, on average, the total amount of energy transferred from the energy-containing scales, and cascaded though the inertial scales, would account for the total that eventually emerges as dissipation on protons, electrons, and minor ions (see, e.g., Wu et al. 2013; Matthaeus et al. 2016).

A recent study of turbulence in the Earth's magnetosheath indeed demonstrates that the estimate of MHD-scale energy decay rate derived from the von Kármán law at the large scales, and the estimate from the third-order law in the inertial scales, agree very well (Bandyopadhyay et al. 2018a). Here, we carry out a similar third-order law estimate of inertial range energy transfer and compare with the von Kármán decay rate using *PSP* data from the first orbit, closer to the Sun than any previous spacecraft mission.

In this paper, we will address two main questions: First, what is the average energy decay rate close to the Sun, within 0.3 au ($60\,R_\odot$)? Second, is there consistency between the cascade rate obtained at the energy-containing scales, evaluated from the von Kármán law, and that estimated from the third-order law at inertial range scales?

Regarding the first point, from theoretical expectations and numerical simulations, there is growing support for substantial plasma heating in close proximity of the corona, an effect that is possibly a result of a turbulent cascade (Matthaeus et al. 1999; Verdini et al. 2009). However, in the absence of any in situ measurement closer than 0.3 au, estimates remained indirect, until now. During its first solar encounter (E1), NASA's *Parker Solar Probe* (*PSP*) (Fox et al. 2016), sampled the young solar wind in this uncharted territory of the heliosphere, ranging from $54\,R_\odot$ to $36\,R_\odot$. We report below evidence for substantial heating of the plasma near *PSP*'s first perihelion.

Our second main question is a natural consequence of the nearly incompressible nature of solar wind turbulence (Zank & Matthaeus 1992), along with the second Kolmogorov hypothesis: The presence of a scale-invariant incompressive energy flux for some range of length scales suggests an inertial range cascade that continues in a conservative fashion the transfer initiated at the energy containing scales. This Kolmogorov conjecture has been tested both directly and indirectly in MHD fluids, and also in weakly collisional plasmas. Nevertheless, it has not been clear how well these conclusions hold near the corona in the very young solar wind. The present analysis of *PSP* data during the first solar encounter demonstrates a good correspondence of the von Kármán and inertial-range cascade rates in the inner-heliospheric solar wind.

2. Data Selection and Method

Our analysis employs magnetic field measurements by the FIELDS (Bale et al. 2016) fluxgate magnetometer (MAG), along with proton velocity and density data from the Solar Probe Cup (SPC; Case et al. 2020) of the SWEAP instrument suite (Kasper et al. 2016). Although both instruments perform measurements all through the orbits, the data collection rate is relatively low for most of the orbits when the spacecraft is far from the Sun. The primary science-data collection, at a high cadence, occurs during the encounter phase of each orbit at $R \leqslant 54\,R_\odot$(0.25 au). The first encounter extends from 2018 October 31 to 2018 November 12, with the first perihelion occurring at 03:27 UT on 2018 November 6. The initial and final days do not have full coverage of the high-time-resolution data, so we perform the analysis on data obtained between 2018 November 1 and 2018 November 10. In particular, Level-two (L2) FIELDS and Level-three (L3i) data from the SWEAP archives are used in this paper. The time cadence of the SPC moments varies between 1 NYHz and 4 NYHz, where 1 NYHz (New York Hz) is the inverse of 1 NY sec (New York second), which is approximately equal to 0.874 s (for an exact definition and more details, see Bale et al. 2016). The native cadence of FIELDS/MAG magnetic field varies from ≈2.3 to 293 samples per second over E1. To generate a uniform time series, we resample all the variables (SPC and FIELDS) to 1 NYHz cadence. Some spurious spikes in the SPC moments, which are remnants of poor quality of fits, are removed.

To compute Elsasser variables from the resampled data, it is necessary to decide how the density is to be handled to produce a physically meaningful conversion of magnetic field to Alfvén speed units. In S.I. units, we have

$$\boldsymbol{V}_{\rm A} = \frac{\boldsymbol{B}}{\sqrt{\mu_0 m_{\rm p} n_{\rm p}}}, \tag{1}$$

where μ_0 is the magnetic permeability of vacuum, $m_{\rm p}$ is the proton mass, and $n_{\rm p}$ is the number density of protons. This conversion is to be performed with some care. In the strictly incompressible case, $n_{\rm p}$ is constant, so, in solar wind studies, one typically uses the value of $n_{\rm p}$ averaged over the whole interval. But very long-term averages can miss local effects. On the other hand, single-time values may overestimate effects of Alfvén speed gradients. Large local variations of density do not imply a possibility of different point-wise Alfvén waves. An inertial range Alfvén wave and corresponding Alfvén speed should be defined over a reasonably large scale, one over which an MHD Alfvén wave can exist and propagate. Hence, we use an approach in which the density is averaged over a few correlation times to convert magnetic field fluctuations into Alfvénic units.

The correlation time during E1 is around $\tau_{\rm corr} \sim$ 300–600 s. These values of correlation time imply that a rolling average of 1250 s covers about two to four characteristic timescales through E1. Therefore, we use this rolling-averaged density to compute the Alfvén velocity, and subsequently, to obtain the Elsasser variables. See Figure 1 and related discussions in Parashar et al. (2020) for more details.

Another subtle complexity arises due to the presence of alpha particles in the ion population. While solar wind alpha particles are a minority population (e.g., Kasper et al. 2007) in terms of their number densities, they are important in terms of their mass contribution (e.g., Robbins et al. 1970; Kasper et al. 2007; Stansby et al. 2019). So the alpha particles can have a large effect on the estimation of the denominator in Equation (1). Since alpha-particle abundance ratios are currently unavailable, we repeat the analysis assuming a 5%

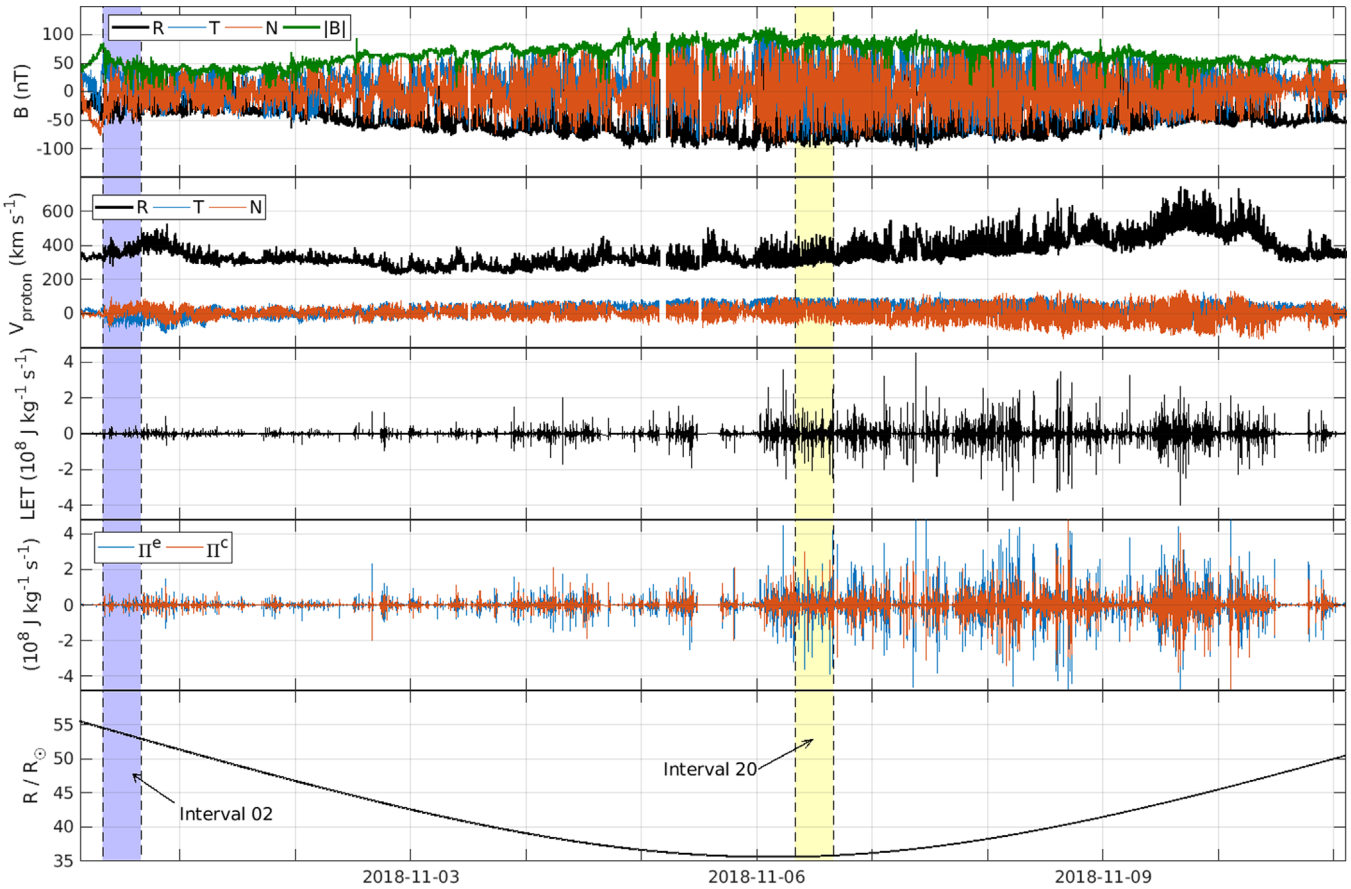

Figure 1. From the top: time series plot of magnetic field components, proton velocity components; the local energy transfer (LET) rate proxy, $\Pi(\ell,t)$, obtained from the unaveraged Yaglom law, Equation (5), for a lag of $\ell \approx 500\, d_i$; the two terms (Equation (7)) of the LET; and the distance of the spacecraft from the Sun, in units of solar radius for the first *PSP* encounter. The two intervals, discussed in detail in the text, are marked by blue (interval 02) and yellow (interval 20) highlighted parts.

alpha-particle abundance by number. However, repeating the analyses this does not change the results significantly (within ±15%). At this stage, a normalization of the Alfvén speed (Equation (1)) taking into account alpha-particle drifts and pressure anisotropies (Barnes 1979; Alterman et al. 2018) is not feasible with the currently available data. However, here we also recall our method of normalizing. Since we are averaging density over roughly a correlation scale, the pressure/temperature anisotropy would also need to be averaged. It is rather certain that the temperature anisotropy will have an average very close to unity when averaged this way, so we anticipate that the effect would be negligible.

We divide E1 (∼10 days) into 8 hr subintervals and perform the analysis on each 8 hr sample individually, labeling each according to its sequence since the beginning of the encounter (2018 October 31), when the spacecraft first crossed below 54 $R_\odot$ (0.25 au). So, for example, interval 2 ranges from 08:00:00 to 16:00:00 UTC, on 2018 October 31 and interval 20 is between 08:00:00 and 16:00:00 UTC, on 2018 November 6. The two subintervals are highlighted in Figure 1. These two subintervals are reported and discussed in detail as specific samples for demonstration in the following sections; interval 02 being near the beginning of E1 at $R \approx 54\, R_\odot$ and interval 20 near the first perihelion $R \approx 36\, R_\odot$. Later, we show the energy decay rates for all the subintervals.

3. Inertial Range

To estimate the energy cascade rate at the inertial scales, ϵ, we use the Kolmogorov–Yaglom law, extended to isotropic MHD (Politano & Pouquet 1998a, 1998b),

$$Y^{\pm}(\ell) = -\frac{4}{3}\epsilon^{\pm}\ell, \tag{2}$$

where, $Y^{\pm}(\ell) = \langle \hat{\ell} \cdot \Delta \boldsymbol{Z}^{\mp}(\boldsymbol{r}, \ell) |\Delta \boldsymbol{Z}^{\pm}(\boldsymbol{r}, \ell)|^2 \rangle$, are the mixed third-order structure functions. Here, $\Delta \boldsymbol{Z}^{\pm}(\boldsymbol{r}, \ell) = \boldsymbol{Z}^{\pm}(\boldsymbol{r} + \ell) - \boldsymbol{Z}^{\pm}(\boldsymbol{r})$ are the increments of Elsasser variables at position $\boldsymbol{r}$ and spatial lag ℓ, and $\langle \cdots \rangle$ denotes spatial averaging. The Elsasser variables are defined as

$$\boldsymbol{Z}^{\pm} = \boldsymbol{V} \pm \boldsymbol{V}_{\rm A}, \tag{3}$$

where $\boldsymbol{V}$ is the plasma (proton) velocity. The variables $\epsilon^{\pm}$ in Equation (2), denote the mean decay rate of the respective Elsasser energies (per units mass): $\epsilon^{\pm} = d(Z^{\pm})^2/dt$; where $Z^{\pm}$ are the rms fluctuation values of the Elsasser fields. The total (kinetic + magnetic) energy decay rate can be calculated as $\epsilon = (\epsilon^{+} + \epsilon^{-})/2$. For single-spacecraft observations, the structure functions are computed for different temporal lags τ. We then use Taylor's "frozen-in" flow hypothesis (Taylor 1938) to interpret the temporal lags as spatial lags:

$$\ell = -\langle \boldsymbol{V} \rangle \tau. \tag{4}$$

Here, $\langle\cdots\rangle$ represents temporal averaging, further interpreted as spatial averaging using Taylor's hypothesis. The Taylor hypothesis can be applied if the sampled structures convect past the spacecraft sufficiently fast so that the nonlinear evolution is negligible during the transition. For MHD-scale turbulent fluctuations, such a condition is met if the mean radial flow speed of the plasma, in the spacecraft frame, is super-Alfvénic (Jokipii 1973). A comparison of the solar wind speed to Alfvén speed for E1 shows that $|\boldsymbol{V}|/|\boldsymbol{V}_{\rm A}| \sim 3$–4, marginally allowing us to use the Taylor hypothesis. A detailed study of Taylor's hypothesis for E1 is reported in A. Chasapis et al. (2019, in preparation; also see Parashar et al. 2020).

The presence of a strong mean-magnetic field in the solar wind creates various kinds of anisotropy (Horbury et al. 2012; Oughton et al. 2015). However, in cases where the isotropic PP98 formulation has been compared to a fully anisotropic determination, it is found that the implied cascade rates compare rather well (Osman et al. 2011; Verdini et al. 2015). Regarding this well-known lack of isotropy in the solar wind, we note that apart from the magnetic field direction, other preferred directions may impose influences on the turbulence. Notable among these is the radial direction (Völk & Aplers 1973; Dong et al. 2014; Verdini & Grappin 2015) which, due to expansion effects, may violate even the less restrictive assumption of axisymmetry (Leamon et al. 1998; Chen et al. 2012; Vech & Chen 2016; Roberts et al. 2017). In spite of these caveats, lacking clear alternatives to the use of the isotropic form of the third-order relation, we proceed using the Politano–Pouquet formulation as an approximation.

The third-order law (Equation (2)) calculates the average energy transfer rate per unit mass, at a given scale ℓ. Here, the average implies an ensemble mean, approximated here as a time average along the one-dimension sampled by the spacecraft. Recently, the local energy transfer rate (LET) dependent on scale ℓ has been examined (approximately) by using as a surrogate the unaveraged third-order structure function that appears in the third-order law (Sorriso-Valvo et al. 2018a, 2018b; Kuzzay et al. 2019),

$$\mathcal{Y}^{\pm}(\ell, \boldsymbol{r}) = -\frac{4}{3}\Pi^{\pm}(\ell, \boldsymbol{r})\ell, \tag{5}$$

where, $\mathcal{Y}^{\pm}(\ell, \boldsymbol{r}) = \hat{\ell} \cdot \Delta\boldsymbol{Z}^{\mp}(\boldsymbol{r}, \ell)|\Delta\boldsymbol{Z}^{\pm}(\boldsymbol{r}, \ell)|^2$ is the unaveraged kernel of the third-order law (Equation (2)). Now, $\Pi^{\pm}(\ell, \boldsymbol{r})$ acts as a proxy for the respective Elsasser energy flux, for a length scale of magnitude ℓ, at a position of $\boldsymbol{r}$. Alternatively, for single-spacecraft observations we can express this as $\Pi^{\pm}(\ell, t)$, where the time t is related to $\boldsymbol{r}$ in a solar wind frame by Taylor's hypothesis (Equation (4)). As usual, the total rate of local transfer of energy is given by averaging the LET for the two Elsasser fields:

$$\Pi = \frac{1}{2}(\Pi^{+} + \Pi^{-}). \tag{6}$$

When averaged over a sufficiently large number of samples, for different positions $\boldsymbol{r}$ (or time t), Π reduces to the energy flux ϵ. The LET can also be written as

$$\Pi = \frac{1}{2}(\Pi^{\rm e} + \Pi^{\rm c}), \tag{7}$$

where, $\Pi^{\rm e} = (-3/4\ell)[2\,\hat{\ell} \cdot \Delta\boldsymbol{V}(\Delta\boldsymbol{V}^2 + \Delta\boldsymbol{V}_{\rm A}^2)]$, is associated with the energy advected by the velocity, and $\Pi^{\rm c} = (-3/4\ell)[-4\,\hat{\ell} \cdot \Delta\boldsymbol{V}_{\rm A}(\Delta\boldsymbol{V} \cdot \Delta\boldsymbol{V}_{\rm A})]$, is associated with the cross-helicity coupled to the longitudinal magnetic field.

The bottom panel of Figure 1 shows the LET for E1 by *PSP*. The LET as shown is calculated for an arbitrary lag of $\ell \approx 500\,d_{\rm i}$, which is well within the inertial range of scales. The proton-inertial length, $d_{\rm i}$, is defined as $d_{\rm i} = c/\omega_{\rm pi} = \sqrt{m_{\rm p}\epsilon_0 c^2/n_{\rm p}e^2}$, where c is the speed of light in vacuum, $\omega_{\rm pi}$ is the proton plasma frequency, ϵ_0 is the vacuum permittivity, and e is the proton charge. This choice of length scale ($\approx 500\,d_{\rm i}$) has no specific motivation other than being far from the kinetic ($\sim d_{\rm i}$), as well as the energy-containing scales ($\sim 10^4\,d_{\rm i}$). Use of other lags in the inertial range produces similar results. From the time series of LET, it is clear that the local energy flux is highly intermittent, with sharp variations in fluctuation values, both positive and negative. Note that there is a striking asymmetry in the LET fluctuations, before and after the first perihelion on 2018 November 6. This asymmetry is also observed in other *PSP* E1 studies and is primarily attributable to changes in the nature of the solar wind during the encounter. The solar wind velocity is remarkably slow in the first half and more closely resembles fast solar wind in the second half. We note here that the alpha-particle abundances are known to vary with the wind speed (Kasper et al. 2007). So the Elsasser variables in the fast-wind intervals may be subjected to a larger error due to higher alpha abundances than in the slow wind. However, as mentioned earlier in the paper, a 5% alpha population does not change the results significantly, so we do not expect that the differences in the inbound and outbound regions are due to underestimating the mass.

If there exists a constant energy flux across the inertial range of length scales, the mixed, third-order structure function on the left-hand side of Equation (2) is proportional to the length scale ℓ on the right-hand side. Therefore, by fitting a straight line to Equation (2), for a suitable range of scales, one can extract the energy cascade rate. Figure 2 plots the third-order structure function ($Y = (Y^{+} + Y^{-})/2$) against length scale in units of proton-inertial scale ($d_{\rm i}$) for two 8 hr subintervals. The top panel shows the structure function for the second subinterval in E1. A linear scaling is shown for reference. By fitting a straight line, the value of ϵ is obtained as 5×10^4 J kg^{-1} s^{-1}, and the uncertainty from the fitting is 2400 J kg^{-1} s^{-1}. We repeat the procedure for a subinterval near the perihelion, a distance of $\sim 36\,R_{\odot}$. Again, a rough linear scaling can be observed, yielding a decay rate of 2×10^5 J kg^{-1} s^{-1}, with an uncertainty of 1.5×10^4 J kg^{-1} s^{-1}. Table 1 reports these estimates. We perform the same analysis for each 8 hr subinterval for E1. Not every case exhibits a linear scaling, and for those 7 intervals from a total of 34 intervals, we report only the von Kármán decay estimate of turbulent energy-dissipation rate, as described in the next section.

4. Energy Containing Scale

We expect that the global decay rate is controlled, to a reasonable level of approximation, by a von Kármán decay law, generalized to MHD (Hossain et al. 1995; Wan et al. 2012; Bandyopadhyay et al. 2019),

$$\epsilon^{\pm} = -\frac{d(Z^{\pm})^2}{dt} = \alpha_{\pm}\frac{(Z^{\pm})^2 Z^{\mp}}{L_{\pm}}, \tag{8}$$

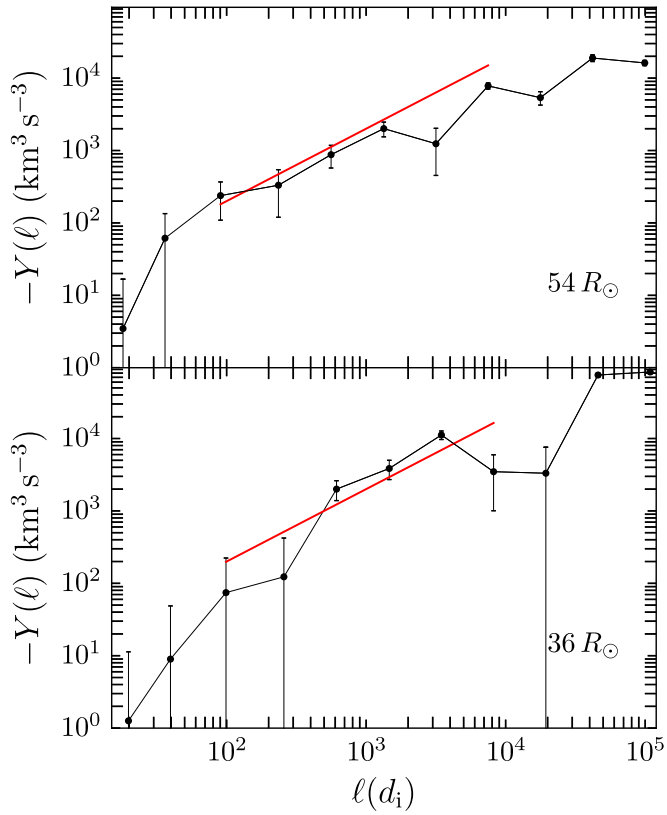

Figure 2. Scaling behavior of the third-order structure function as a function of the (Taylor shifted) length scale in units of ion-inertial length for two different periods we examined. Top: interval 2 on 2018 October 31, from 08:00:00 to 16:00:00 UTC; $R = 54\ R_\odot$. Bottom: interval 20, near the Perihelion, 2018 November 6, from 08:00:00 to 16:00:00 UTC; $R = 36\ R_\odot$. The thick red lines correspond to linear scaling laws for reference. The error bars are calculated by $\sigma/\sqrt{m}$, where σ is the standard deviation and m is the number of points, used to calculate the mean.

Table 1
Inertial Range Cascade Rate Estimates

Interval	R ($R_\odot$)	ϵ (J kg^{-1} s^{-1})
02	54	$(5.0 \pm 0.2) \times 10^4$
20	36	$(2.0 \pm 0.2) \times 10^5$

Note. These are based on PP98 MHD adaptation of the Yaglom law.

where $\alpha_\pm$ are positive constants and $Z^\pm$ are the rms fluctuation values of the Elsasser variables.

The similarity length scales $L_\pm$ in Equation (8) are the characteristic scales of the energy containing eddies. Usually, a natural choice for the similarity scales are the associated correlation lengths, computed from the two-point correlation functions of the Elsasser variables. Although, there have been some studies showing that this association may not always be appropriate (Krishna Jagarlamudi et al. 2019).

The basis of the estimate is determination of the trace of the two-point, single-time correlation tensor, which under suitable conditions, and assuming the Taylor hypothesis, is approximately determined by the measured two-time correlation. The trace of the correlation tensors, computed from the Elsasser

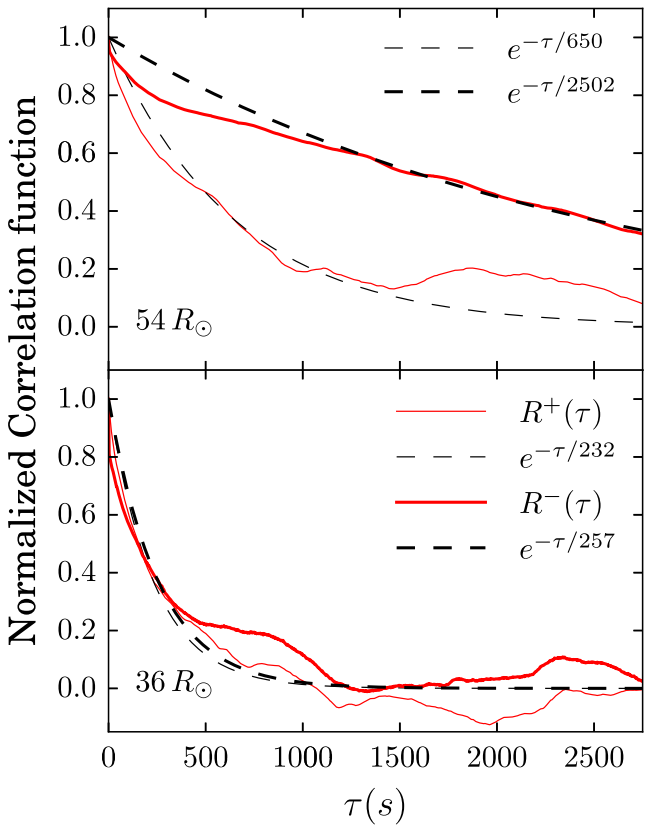

Figure 3. Correlation function vs. time lag (seconds) for the Elsasser variables and the corresponding exponential fits for estimation of correlation time. Top: interval 02 on 2018 October 31, from 08:00:00 to 16:00:00 UTC; $R = 54\ R_\odot$. Bottom: interval 20, near the Perihelion, 2018 November 06, from 08:00:00 to 16:00:00 UTC; $R = 36\ R_\odot$.

variables, is given by

$$R^\pm(\tau) = \langle \mathbf{Z}^\pm(t) \cdot \mathbf{Z}^\pm(t+\tau) \rangle_T, \tag{9}$$

where $\langle \cdots \rangle_T$ denotes a time average, usually over the total time span of the data. We use the standard Blackman–Tukey method, with subtraction of the local mean, to evaluate Equation (9). Although the standard definition of correlation scale is given by an integral over the correlation function, in practice, especially when there is substantial low frequency power present, it is advantageous to employ an alternative "1/e" definition (Smith et al. 2001), namely

$$R^\pm(\tau^\pm)/R^\pm(0) = \frac{1}{e}, \tag{10}$$

$$L_\pm = |\langle \boldsymbol{V} \rangle| \tau^\pm, \tag{11}$$

where Equation (11) exploits the Taylor hypothesis. Qualitatively, for some spectra with fairly good statistical weight, the reciprocal correlation length corresponds to the low frequency "break" in the inertial range power law.

Proceeding accordingly, we first compute the Elsasser variables, $\mathbf{Z}^\pm$, based on the proton velocity. We then calculate normalized correlation functions for a maximum lag of one-tenth of the total data set. In Figure 3, we show the normalized correlation function for each Elsasser variable for the two subintervals at heliocentric distances of $R = 54\ R_\odot$ and $36\ R_\odot$, respectively. Fitting an exponential function to each of the normalized correlation function yields correlation time

Table 2
Derived Variables

Interval	Z^+ (km s^{-1})	L_+ (km)	Z^- (km s^{-1})	L_- (km)	σ_c
02	88	211×10^3	54	811×10^3	0.45
20	126	58×10^3	48.7	65×10^3	0.74

Note. Elsasser amplitudes $Z^{\pm}$, correlation lengths $L_{\pm}$, and normalized cross-helicity defined as $\sigma_c = [(Z^+)^2 - (Z^-)^2]/[(Z^+)^2 + (Z^-)^2]$.

$\tau^+ = 650$ s and $\tau^- = 2502$ s for the subinterval at $R = 54\,R_\odot$, and $\tau^+ = 232$ s and $\tau^- = 257$ s for the subinterval at $R = 36\,R_\odot$. Using the mean flow speed for these two intervals, the deduced correlation lengths are $L_+ = 211 \times 10^3$ km and $L_- = 811 \times 10^3$ km for interval 02, and $L_+ = 58 \times 10^3$ km and $L_- = 65 \times 10^3$ km for interval 20. Note that these correlation times are about 10−50 times shorter than the analogous time and length scales for 1 au solar wind (Matthaeus & Goldstein 1982a), as anticipated by observations and theory (e.g., Breech et al. 2008; Ruiz et al. 2014; Zank et al. 2017). We report these length scales along with some other obtained quantities in Table 2.

Using the obtained Elsasser amplitudes and correlation lengths, we calculate the estimates of energy decay rate from the von Kármán law, as outlined in Equation (8). We use $\alpha_+ \approx \alpha_- = 0.03$. These values are derived from the dimensionless dissipation rate, C_ϵ, in MHD turbulence: $\alpha_\pm = 2C_\epsilon/9\sqrt{3}$ (Usmanov et al. 2014). The precise values of $\alpha_\pm$ depend on several parameters, e.g., the mean-magnetic-field strength, cross-helicity, and magnetic helicity, but usually remain close to the generic values used here (Matthaeus et al. 2004; Linkmann et al. 2015, 2017; Bandyopadhyay et al. 2018b).

The largest source of uncertainty in these calculations is due to the assumption of homogeneity. To estimate the uncertainties associated with each of the von Kármán decay estimate, we divide each 8 hr interval further into two 4 hr parts and calculate the amplitude of the Elsasser variables in the two halves. From those values of Elsasser amplitude, we calculate the average energy decay rate, and the difference with the original decay rate, estimated from the 8 hr interval, is reported as the uncertainty. The values of the energy decay rate ϵ found in this analysis, for the two subintervals, are reported in Table 3. A comparison with Table 1 affirms that the estimated values are fairly close.

5. Estimates from Global Simulation

In this section, we compare the *PSP* measured cascade rates, as derived in the earlier sections, with global solar corona and solar wind simulations (Usmanov et al. 2018; Chhiber et al. 2019). The simulations are three-dimensional, MHD-based models with self-consistent turbulence transport and heating. For comparison with *PSP* observation, we employ two simulation runs, distinguished by the magnetic field boundary condition at the coronal base. In the first run, a Sun-centered, untilted dipole magnetic field is used for the inner surface magnetic field boundary condition. A zero or small tilt of dipole magnetic field with respect to the solar rotation axis is often associated with the conditions of solar minimum, which *PSP* sampled during its first encounter. The second run is obtained by using the magnetic field boundary condition from 2018 November magnetogram data (Carrington Rotation 2210), normalized appropriately. More details about these simulations can be found in Chhiber et al. (2019).

Table 3
Global Decay Rate Estimates from von Kármán Law

Interval	R ($R_\odot$)	ϵ (J kg^{-1} s^{-1})
02	54	$(3.0 \pm 0.7) \times 10^4$
20	36	$(2.00 \pm 0.07) \times 10^5$

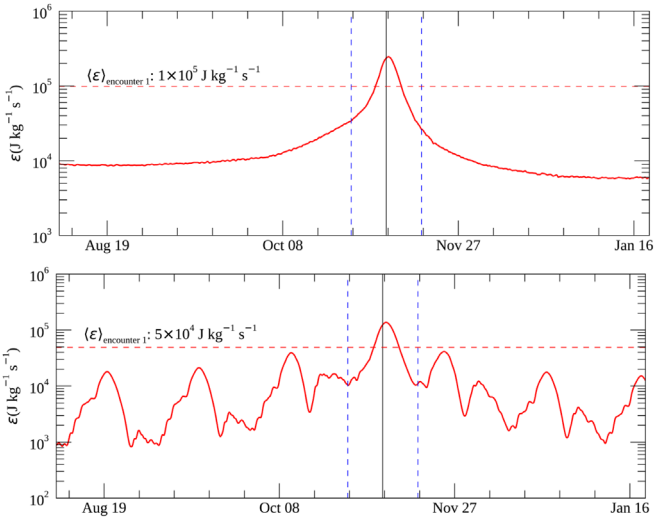

Figure 4. Results from a global simulation. Top: untilted dipole simulation, bottom: 2018, November magnetogram simulation. The first solar encounter (E1) is highlighted as the region within blue dashed lines and the first perihelion is shown as the solid vertical line. The average heating rate during the encounter is indicated by a dashed, horizontal line in each case.

Figure 4 shows a profile of heating rates computed using a von Kármán-like phenomenology from the global heliospheric simulations. Here, the simulated data are sampled along a trajectory similar to that of *PSP* using an untilted dipole (top panel), and using a 2018 November magnetogram (bottom panel). The average values for the encounter are shown as horizontal lines. It is apparent that the expectations based on the simulations correspond well to the observed values. E1 is indicated by the two dashed vertical lines and the solid vertical line marks the first perihelion.

For a more direct comparison of the two kinds of estimates from *PSP* results, along with the simulation predictions, in Figure 5, we plot the different estimates of energy decay rate for E1. The first perihelion is shown as a dashed vertical line, for reference. The thin, blue line and the thick, green line represent the simulation results for the boundary condition of a dipole magnetic field with 0° tilt with respect to the solar rotation axis and that obtained from 2018 November magnetogram data. The red line with triangular symbols represents the values obtained from the third-order law, whenever a linear scaling is found. The orange line with square symbols represents the values calculated using von Kármán phenomenology.

Evidently, there is a fairly good level of agreement among the different estimates of heating rate. The average heating rate is maximum near the perihelion but is generally higher for the second half of the encounter and the consistency is also better

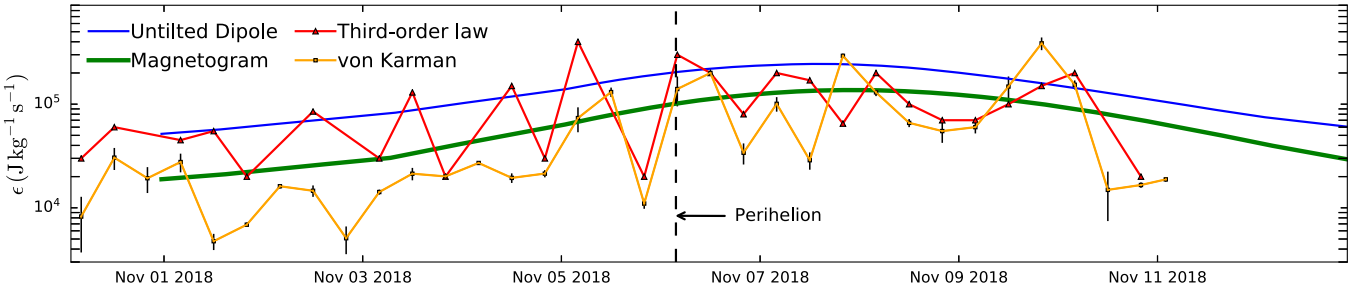

Figure 5. Estimates of the energy decay rate from third-order law (red line with triangles) and von Kármán decay rate (orange line with black squares) for E1. The error bars, when they are larger than the symbols, are shown as black, vertical bars. Also shown are the heating rate estimates from a global simulation model along a virtual *PSP* trajectory, for the untilted dipole condition (thin blue line) and a 2018 November magnetogram simulation (thick green line). The perihelion is shown as a dashed vertical line.

during this period. Possible explanations for this observation are discussed later.

6. Conclusions

The first orbit by *PSP*, particularly during its voyage when the spacecraft was closer than 0.25 au to the Sun, presents several novel observations, e.g., corotational flows (Kasper et al. 2019), rapid polarity reversals in a mostly radial magnetic field (the so-called "switchbacks" (Bale et al. 2019; Dudok de Wit et al. 2020), numerous sharp, discrete Alfvénic impulses with an antisunward propagating direction (the so-called "spikes"; Horbury et al. 2020), suprathermal population (McComas et al. 2019). In this paper, taking advantage of this unique opportunity to make in situ observations at unprecedented close distances to the solar corona, we have performed some first basic turbulence cascade rate statistics, analyzing the full E1 data as an ensemble of fluctuations.

Although much emphasis is often placed on the significance of the spectral slope ($E(k) \sim k^{-5/3}$, $k^{-3/2}$), the scaling of mixed, third-order structure functions (Equation (2)) is considered a more direct indication of inertial range cascade in turbulent plasma. For most of the intervals analyzed here, the averaged third-order structure functions exhibit linear scaling with length scale.

We use two estimates of energy decay rate at the MHD scales: a von Kármán decay law and a Politano–Pouquet third-order law. The two estimates are fairly consistent. However, from Figure 5, clearly, the agreement is better for the outbound leg of E1. This effect may be attributed to the fact that, overall the fluctuation amplitudes are higher in the fast solar wind plasma for the later part of E1. The local energy transfer rate is larger in the parts that appear to be more Alfvénic. The region after 2018 November 9 has a reasonably low speed (under 400 km s^{-1} for the first part) but high Alfvénicity, indicating that some part of this is a sample of Alfvénic slow wind (D'Amicis et al. 2018). Typically, the slow solar wind is observed to be more intermittent (e.g., Bruno et al. 2003). The LET has been shown to be related to the partial variance of increment PVI statistics (Sorriso-Valvo et al. 2018a). If one assumes that the slow wind is populated with more coherent structures, then the larger fluctuations of LET seen in the fast-wind periods are most likely due to Alfvénic fluctuations. We note, however, that the Alfvénicity is not perfect, and that turbulence may be fairly active in these regions since the required mixture of + and − Elsasser amplitudes is present in these epochs (Parashar et al. 2020). Additional studies are required to reach a definite conclusion.

We also see that the Usmanov et al. (2018) global-simulation model predicts the heating rate reasonably well in comparison with the *PSP* observations. Some contextual comparisons with results from previous in situ observations are also in order. We have mentioned previously that the average cascade rate for 1 au solar wind plasma is approximately $\sim 10^3$ J kg^{-1} s^{-1}, the particular value depending on the specific solar wind conditions (Coburn et al. 2015). Using *Helios* 2 data, Hellinger et al. (2013) evaluates the heating rate at 0.3 au slow solar wind as $\sim 10^{-15}$ J m^{-3} s^{-1} $\equiv$ 6000 J kg^{-1} s^{-1}, which is close to the value of $\sim 10^4$ J kg^{-1} s^{-1} obtained at 0.25 au in the slow wind by *PSP*, near the beginning of E1. The energy decay rate becomes progressively larger closer to the perihelion and the highest obtained values are almost comparable to the values obtained for the shocked plasma in Earth's magnetosheath (Bandyopadhyay et al. 2018a; Hadid et al. 2018). This large value of energy cascade rate is presumably due to the strong driving process occurring closer to the corona. There are some peculiarities about E1. These studies, unlike the ones with *Helios* or Wind data, do not have the statistical capability to investigate underlying parametric dependences. Incorporating more data from future *PSP* orbits and Solar Orbiter (Müller et al. 2013), capturing more kinds of solar wind, will make the scenario clearer.

The theory of MHD turbulence, and consequently, the phenomenologies discussed here, are statistical in nature (Monin & Yaglom 1971, 1975). Accordingly, the heating rates obtained here are independent of any specific dissipation mechanism and are not applicable for individual events. However, a model of stochastic heating mechanism (Martinovic et al. 2020) in this volume, accounts for a significant fraction of the heating rates reported in this study, suggesting that stochastic heating may be a major contribution to overall proton heating in these regions. Future comparisons with other processes, e.g., reconnection, ion-cyclotron damping, and Landau damping, will be useful, using measurements of the particle velocity distribution function (He et al. 2015) or methods such as field-particle correlations (Klein & Howes 2016).

The present study is not without limitations and those deserve to be addressed at this point. The two decay laws we employed, are derived on the basis of homogeneity and stationarity (Politano & Pouquet 1998a, 1998b; Wan et al. 2012). Whether solar wind fluctuations, particularly the ones sampled by *PSP* in the inner heliosphere, satisfy the conditions of weak stationarity, is not entirely clear and requires more rigorous investigation (Matthaeus & Goldstein 1982b; Chhiber et al. 2020; Dudok de Wit et al. 2020; Parashar et al. 2020). In

regions close to the corona, expansion effects may become important, but they are ignored in the two phenomenologies used here. Finally, we have not explored the statistics of LET here. More detailed studies that pursue these considerations await.

Parker Solar Probe was designed, built, and is now operated by the Johns Hopkins Applied Physics Laboratory as part of NASA's Living with a Star (LWS) program (contract NNN06AA01C). Support from the LWS management and technical team has played a critical role in the success of the *Parker Solar Probe* mission. This research was partially supported by the *Parker Solar Probe* Plus project through Princeton/IS⊙IS subcontract SUB0000165, NASA grant 80NSSC18K1210, NASA HSR grant 80NSSC18K1648, NSF-SHINE AGS-1460130, and in part by grant RTA6280002 from Thailand Science Research and Innovation. S.D.B. acknowledges the support of the Leverhulme Trust Visiting Professorship program.

ORCID iDs

Riddhi Bandyopadhyay https://orcid.org/0000-0002-6962-0959
M. L. Goldstein https://orcid.org/0000-0002-5317-988X
B. A. Maruca https://orcid.org/0000-0002-2229-5618
W. H. Matthaeus https://orcid.org/0000-0001-7224-6024
T. N. Parashar https://orcid.org/0000-0003-0602-8381
D. Ruffolo https://orcid.org/0000-0003-3414-9666
R. Chhiber https://orcid.org/0000-0002-7174-6948
A. Usmanov https://orcid.org/0000-0002-0209-152X
A. Chasapis https://orcid.org/0000-0001-8478-5797
R. Qudsi https://orcid.org/0000-0001-8358-0482
Stuart D. Bale https://orcid.org/0000-0002-1989-3596
J. W. Bonnell https://orcid.org/0000-0002-0675-7907
Thierry Dudok de Wit https://orcid.org/0000-0002-4401-0943
Keith Goetz https://orcid.org/0000-0003-0420-3633
Robert J. MacDowall https://orcid.org/0000-0003-3112-4201
David M. Malaspina https://orcid.org/0000-0003-1191-1558
Marc Pulupa https://orcid.org/0000-0002-1573-7457
J. C. Kasper https://orcid.org/0000-0002-7077-930X
K. E. Korreck https://orcid.org/0000-0001-6095-2490
A. W. Case https://orcid.org/0000-0002-3520-4041
M. Stevens https://orcid.org/0000-0002-7728-0085
P. Whittlesey https://orcid.org/0000-0002-7287-5098
K. G. Klein https://orcid.org/0000-0001-6038-1923
M. Velli https://orcid.org/0000-0002-2381-3106

References

Alterman, B. L., Kasper, J. C., Stevens, M. L., & Koval, A. 2018, ApJ, 864, 112
Bale, S. D., Goetz, K., Harvey, P. R., et al. 2016, SSRv, 204, 49
Bale, S. D., Badman, S. T., Bonnell, J. W., et al. 2019, Natur, 576, 237
Bandyopadhyay, R., Chasapis, A., Chhiber, R., et al. 2018a, ApJ, 866, 106
Bandyopadhyay, R., Matthaeus, W. H., Oughton, S., & Wan, M. 2019, JFM, 876, 5
Bandyopadhyay, R., Oughton, S., Wan, M., et al. 2018b, PhRvX, 8, 041052
Barnes, A. 1979, in Solar System Plasma Physics, ed. E. N. Parker, C. F. Kennel, & L. J. Lanzerotti (Amsterdam: North-Holland), 251
Breech, B., Matthaeus, W. H., Minnie, J., et al. 2008, JGRA, 113, 8105
Bruno, R., Carbone, V., Sorriso-Valvo, L., & Bavassano, B. 2003, JGRA, 108, 1130
Case, A. W., Kasper, J. C., Stevens, M. L., et al. 2020, ApJS, doi:10.3847/1538-4365/ab5a7b
Chen, C. H. K., Klein, K. G., & Howes, G. G. 2019, NatCo, 10, 740
Chen, C. H. K., Mallet, A., Schekochihin, A. A., et al. 2012, ApJ, 758, 120
Chhiber, R., Goldstein, M., Maruca, B., et al. 2020, ApJS, doi:10.3847/1538-4365/ab53d2
Chhiber, R., Usmanov, A. V., Matthaeus, W. H., Parashar, T. N., & Goldstein, M. L. 2019, ApJS, 242, 12
Coburn, J. T., Forman, M. A., Smith, C. W., Vasquez, B. J., & Stawarz, J. E. 2015, RSPTA, 373, 20140150
D'Amicis, R., Matteini, L., & Bruno, R. 2018, MNRAS, 483, 4665
de Kármán, T., & Howarth, L. 1938, RSPSA, 164, 192
Dong, Y., Verdini, A., & Grappin, R. 2014, ApJ, 793, 118
Dudok de Wit, T., Krasnoselskikh, V. V., Bale, S. D., et al. 2020, ApJS, doi:10.3847/1538-4365/ab5853
Fox, N. J., Velli, M. C., Bale, S. D., et al. 2016, SSRv, 204, 7
Hadid, L. Z., Sahraoui, F., Galtier, S., & Huang, S. Y. 2018, PhRvL, 120, 055102
He, J., Wang, L., Tu, C., Marsch, E., & Zong, Q. 2015, ApJL, 800, L31
Hellinger, P., Travnicek, P. M., Stverak, S., Matteini, L., & Velli, M. 2013, JGRA, 118, 1351
Hellinger, P., Verdini, A., Landi, S., Franci, L., & Matteini, L. 2018, ApJL, 857, L19
Horbury, T. S., Wicks, R. T., & Chen, C. H. K. 2012, SSRv, 172, 325
Horbury, T. S., Woolley, T., Laker, R., et al. 2020, ApJS, doi:10.3847/1538-4365/ab5b15
Hossain, M., Gray, P. C., Pontius, D. H., Matthaeus, W. H., & Oughton, S. 1995, PhFl, 7, 2886
Jokipii, J. R. 1973, ARA&A, 11, 1
Kasper, J. C., Bale, S. D., Belcher, J. W., et al. 2019, Natur, 576, 228
Kasper, J. C., Abiad, R., Austin, G., et al. 2016, SSRv, 204, 131
Kasper, J. C., Stevens, M. L., Lazarus, A. J., Steinberg, J. T., & Ogilvie, K. W. 2007, ApJ, 660, 901
Klein, K. G., & Howes, G. G. 2016, ApJL, 826, L30
Klein, K. G., Howes, G. G., & Tenbarge, J. M. 2017, JPlPh, 83, 535830401
Kolmogorov, A. N. 1941, DoSSR, 32, 16
Krishna Jagarlamudi, V., Dudok de Wit, T., Krasnoselskikh, V., & Maksimovic, M. 2019, ApJ, 871, 68
Kuzzay, D., Alexandrova, O., & Matteini, L. 2019, PhRvE, 99, 053202
Leamon, R. J., Smith, C. W., Ness, N. F., Matthaeus, W. H., & Wong, H. K. 1998, JGRA, 103, 4775
Linkmann, M., Berera, A., & Goldstraw, E. E. 2017, PhRvE, 95, 013102
Linkmann, M. F., Berera, A., McComb, W. D., & McKay, M. E. 2015, PhRvL, 114, 235001
MacBride, B. T., Forman, M. A., & Smith, C. W. 2005, ESA Spec. Publ., 592, 613
MacBride, B. T., Smith, C. W., & Forman, M. A. 2008, ApJ, 679, 1644
Martinovic, M. M., Klein, K. G., Kasper, J. C., et al. 2020, ApJS, doi:10.3847/1538-4365/ab527f
Matthaeus, W. H., & Goldstein, M. L. 1982a, JGR, 87, 6011
Matthaeus, W. H., & Goldstein, M. L. 1982b, JGRA, 87, 10347
Matthaeus, W. H., Minnie, J., Breech, B., et al. 2004, GeoRL, 31, L12803
Matthaeus, W. H., Parashar, T. N., Wan, M., & Wu, P. 2016, ApJL, 827, L7
Matthaeus, W. H., Zank, G. P., Oughton, S., Mullan, D. J., & Dmitruk, P. 1999, ApJL, 523, L93
McComas, D. J., Christian, E. R., Cohen, C. M. S., et al. 2019, Natur, 576, 223
Mininni, P. D., & Pouquet, A. 2009, PhRvE, 80, 025401
Monin, A. S., & Yaglom, A. M. 1971, Statistical Fluid Mechanics, Vol. 1 (Cambridge, MA: MIT Press)
Monin, A. S., & Yaglom, A. M. 1975, Statistical Fluid Mechanics, Vol. 2 (Cambridge, MA: MIT Press)
Müller, D., Marsden, R. G., St., Cyr, O. C., Gilbert, H. R. & The Solar Orbiter Team 2013, SoPh, 285, 25
Osman, K. T., Wan, M., Matthaeus, W. H., Weygand, J. M., & Dasso, S. 2011, PhRvL, 107, 165001
Oughton, S., Matthaeus, W. H., Wan, M., & Osman, K. T. 2015, RSPTA, 373, 20140152
Parashar, T. N., Goldstein, M. L., Maruca, B. A., et al. 2020, ApJS, doi:10.3847/1538-4365/ab64e6
Politano, H., & Pouquet, A. 1998a, GeoRL, 25, 273
Politano, H., & Pouquet, A. 1998b, PhRvE, 57, R21
Robbins, D. E., Hundhausen, A. J., & Bame, S. J. 1970, JGR, 75, 1178
Roberts, O. W., Narita, Y., & Escoubet, C. P. 2017, ApJL, 851, L11

Ruiz, M. E., Dasso, S., Matthaeus, W. H., & Weygand, J. M. 2014, SoPh, 289, 3917
Smith, C. W., Matthaeus, W. H., Zank, G. P., et al. 2001, JGRA, 106, 8253
Sorriso-Valvo, L., Carbone, F., Perri, S., et al. 2018a, SoPh, 293, 10
Sorriso-Valvo, L., Marino, R., Carbone, V., et al. 2007, PhRvL, 99, 115001
Sorriso-Valvo, L., Perrone, D., Pezzi, O., et al. 2018b, JPlPh, 84, 725840201
Stansby, D., Perrone, D., Matteini, L., Horbury, T. S., & Salem, C. S. 2019, A&A, 623, L2
Stawarz, J. E., Smith, C. W., Vasquez, B. J., Forman, M. A., & MacBride, B. T. 2009, ApJ, 697, 1119
Taylor, G. I. 1938, RSPSA, 164, 476
Usmanov, A. V., Goldstein, M. L., & Matthaeus, W. H. 2014, ApJ, 788, 43
Usmanov, A. V., Matthaeus, W. H., Goldstein, M. L., & Chhiber, R. 2018, ApJ, 865, 25
Vech, D., & Chen, C. H. K. 2016, ApJL, 832, L16
Verdini, A., & Grappin, R. 2015, ApJL, 808, L34
Verdini, A., Grappin, R., Hellinger, P., Landi, S., & Müller, W. C. 2015, ApJ, 804, 119
Verdini, A., Velli, M., Matthaeus, W. H., Oughton, S., & Dmitruk, P. 2009, ApJL, 708, L116
Verma, M. K. 2004, PhR, 401, 229
Völk, H. J., & Aplers, W. 1973, Ap&SS, 20, 267
Wan, M., Oughton, S., Servidio, S., & Matthaeus, W. H. 2012, JFM, 697, 296
Wu, P., Wan, M., Matthaeus, W. H., Shay, M. A., & Swisdak, M. 2013, PhRvL, 111, 121105
Yang, Y., Matthaeus, W. H., Parashar, T. N., et al. 2017, PhPl, 24, 072306
Zank, G. P., Adhikari, L., Hunana, P., et al. 2017, ApJ, 835, 147
Zank, G. P., & Matthaeus, W. H. 1992, JGRA, 97, 17189